


High aspect ratio tilted gratings through local electric field modulation in plasma etching

Journal Article

Author(s):

Shi, Zhitian; Jefimovs, Konstantins; La Magna, Antonino; Stampanoni, Marco; [Romano, Lucia](#) 

Publication date:

2022-06-30

Permanent link:

<https://doi.org/10.3929/ethz-b-000543556>

Rights / license:

[Creative Commons Attribution-NonCommercial-NoDerivatives 4.0 International](#)

Originally published in:

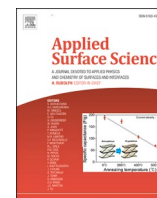
Applied Surface Science 588, <https://doi.org/10.1016/j.apsusc.2022.152938>

Funding acknowledgement:

154472 - Med-XPhase – Phase contrast X-ray imaging as a new diagnostic tool (SNF)

183568 - GI-BCT - Clinical Grating Interferometry Breast Computed Tomography (SNF)

159263 - X-ray phase-contrast micro computed tomography for improved pathology (SNF)



Full Length Article

High aspect ratio tilted gratings through local electric field modulation in plasma etching



Zhitian Shi^{a,b,*}, Konstantins Jefimovs^a, Antonino La Magna^c, Marco Stampanoni^{a,b},
Lucia Romano^{a,b}

^a Paul Scherrer Institut, 5232 Villigen PSI, Switzerland

^b Institute for Biomedical Engineering, ETH Zürich, 8092 Zürich, Switzerland

^c CNR Institute for Microelectronics and Microsystems, VIII Strada, 5, 95121 Catania, Italy

ARTICLE INFO

Keywords:

Plasma etching
High aspect ratio
Tilted etching
Electric field modulation
Diffractive optics
Fan shaped gratings

ABSTRACT

The anisotropic nature of plasma etching is usually exploited to realize vertical nano-/micro- silicon structures by deep reactive ion etching. However, some applications require tilted instead of perpendicular profiles with respect to the substrate. Here, a controlled tilted etching is realized by introducing a set of metal electric field modulator(s), which modify the near sample surface potential. The ions from the plasma body are accelerated under the influence of the distorted electric field, and hit the silicon surface with a certain incident angle. A model is built with finite elements method, taking into account the geometry of the experiment and the chamber conditions during the etching process. The thickness and the inter-distance of Al slabs have been varied in a range of 0.5–3 mm and 10–25 mm, respectively. A tilt angle ranging from 0° to 22.6° has been measured and validates the simulation results, showing that a desired tilt profile can be achieved with a proper parameters tuning. Examples of 1D and 2D modulations are reported with linear and chessboard slanted gratings for X-ray imaging applications.

1. Introduction

Slanted diffraction gratings are used in various photonics devices to perform certain optical functions such as coupling a projected image into a waveguide in displays for augmented and virtual reality applications [1]. In surface relief grating technology [2], nanoimprint is used as replication method of slanted gratings fabricated by ion beam and plasma etching with glancing incidence. Asymmetric groove profiles are very appealing because of very high efficiency in diffractive in-coupling of light into light guides [3] but the glancing ion etching cannot achieve the required precision of a continuous slant angle variation with a grating period in the range of the visible wavelengths. High aspect ratio diffractive optics are used in X-ray imaging applications as active devices for phase and dark field contrast modalities [4] or as focusing elements [5]. X-ray imaging applications would benefit of the tilt modulation in the diffractive optics to cope with divergent beam illumination, which is particularly critical in X-ray tube sources. X-rays emitted from an X-ray tube usually propagate in a cone shape confined space (fan shape if observed in a two dimensional space). Diffractive X-

ray optics are periodic microstructures, whose aspect ratio grows as a function of the X-ray energy because of the weak interaction of X-rays with matter. For example, in grating based X-ray interferometry (XGI) for medical diagnostics at 20 keV X-ray energy [6], the gratings with pitch size in the range of 1–5 μm are made of Si trenches, filled with Au for height higher than 30 μm [7–9], while Au thickness higher than 100 μm [10] are necessary for X-ray dark-field chest radiography, where tube acceleration voltage peak is typically higher than 60 kV [11]. Limited by the available optics fabrication techniques, X-ray imaging systems suffer from the misalignment between the X-ray source emission and the diffractive microstructures. Depending on the imaging application, the device size of the X-ray optical elements can span from few hundreds micrometers (e.g. Fresnel zone plates in X-ray microscopes [5]) to few centimeters (e.g. source gratings in XGI [7]), to tens of centimeters (e.g. analyzing gratings in XGI [6]). With respect to microfabrication for microelectronics devices, the pattern of an X-ray grating occupy a full Si wafer and the precision of pattern definition (pitch and duty cycle) and the pattern transfer over the full area deeply affect the imaging performances, since the angular sensitivity of the

* Corresponding author.

E-mail address: zhitian.shi@psi.ch (Z. Shi).

interferometric system is in the range of 10–100 nrad [7]. The misalignment limitation increases with the aspect ratio of the optical element, reducing the effective area of the diffractive device and its diffraction efficiency, affecting the final field of view and the imaging quality, respectively. We recently demonstrated [12] that an X-ray source grating can be fabricated in such a way that the directionality of the functional microstructures is already matched with the divergent beam of X-ray source as shown in Fig. 1(a). Mechanical bending (Fig. 1b) of the X-ray gratings [13,14] works with Si substrates of few hundred micrometers and moderate bending radiiuses, but it is very critical for the source grating, limiting its position right after the source. Alternatively, the fan-shaped grating has lines etched in a flat silicon substrate with a slant angle modulation, allowing the positioning of the grating very close to the source, with a clear gain in X-ray flux and system total length [12].

Tilted etching has been approached for optical lenses fabrication by using Faraday cages, rotating electrode, angled gas injection, and etc.

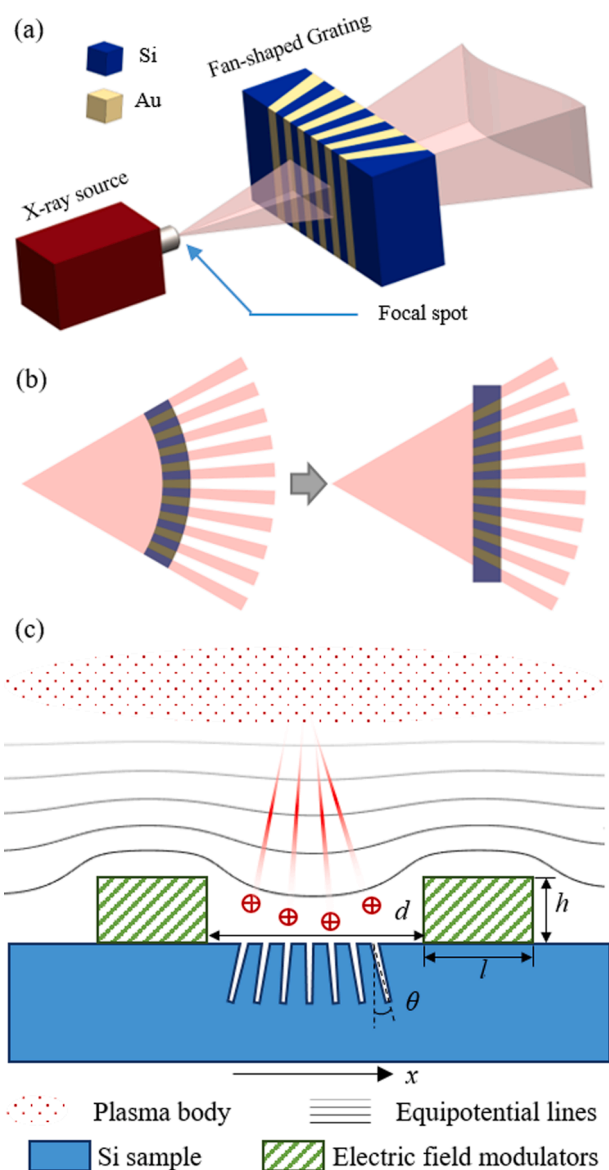


Fig. 1. (a) A Talbot-Lau XGI system with curved gratings for better beam alignment. (b) Concept of replacing the bent G_0 grating with a fan-shaped G_0 grating. (c) Local electric field in presence of an electric field modulator (d the inter-slabs distance, h the slab thickness and l the slab width), and a sketched profile of grating lines with tilted etching θ as a function of position x . The equipotential lines are plotted as curved lines in grey scale.

[15–17]. None of these technologies is suitable for the fabrication of high aspect ratio microstructures with a continuous gradient tilt in the etched trenches. Our method realizes the tilted etching by modulating the electric field during the deep reactive ion etching of a patterned Si substrate. Local electric field modulators (Fig. 1c) locally modify the ion trajectories in order to modulate the ion impinging direction on the patterned substrates as a function of the distance from the modulator. Only plasma etching techniques can benefit of local angular modulation, with respect to conventional [18] or new [19] wet-etching methods. Deep reactive ion etching (DRIE) applications usually require the etching direction to be perpendicular to the substrate as much as possible, and any unwanted tilting should be mitigated [20]. For example, in integrated circuits fabrication, the tilted contact holes at the edge area of the wafer will lead to a direct fail of the entire chip, which decreases the yield and increases the cost [21]. On the other side, applications such as augmented and virtual reality [1], micro-sensors, bioelectrodes or superhydrophobic surfaces, may benefit from tilted components [22–24].

In X-ray imaging, the slant angle modulation becomes an important design parameter, depending on the X-ray source and the relative grating position in the system. Here, a dedicated plasma simulation has been developed to calculate the tilt dependence on the modulator's geometry and the tilt gradient inside the grating patterned area. We show some examples of different modulator shapes, in symmetric and asymmetric configuration. For symmetric bar modulators, we studied the ion trajectories as a function of the modulators distance and the bar height. The simulations have been validated by measuring the local tilt of grating lines in the area between the modulators. We report an experimental demonstration of the DRIE process with one dimensional (1-D) and two dimensional (2-D) electric field modulators aimed at the fabrication of hard X-ray fan-shaped linear and chessboard gratings.

2. Material and methods

2.1. Local electric field modulation

DRIE methods have been used for the fabrication of nano-/micro- Si structures, for their reliable etching profile, quality control and process robustness [25]. Bosch process and cryogenic etching are two of the most frequently DRIE methods that provide relatively high etch rate [26,27]. Cryogenic etching method is used for the etching of structures with feature size in the 100 s nanometers scale. Bosch process is optimized at industrial level for applications with feature size in a wider range of few hundreds of nanometers to few hundreds of micrometers, or even larger, and it is commonly used in the fabrication of integrated circuits, MEMS, optics, sensors, and etc. [10,28–30]. Inductively coupled plasma (ICP) etchers are used to conduct Bosch process, as they provide plasma with higher ionization density, which helps to deliver higher etch rates and better selectivity during the Si etching [31]. Commercial ICP etchers integrate two or more radio frequency (RF) power supplies into their systems, with at least one set of RF generator connected to a flat or solenoid coil as ICP generator, and at least one set of RF power supplies connected to the electrode as capacitive coupled plasma (CCP) generator. Fig. 2(a) schematically shows a common ICP etcher chamber. A turbo pump maintains the chamber pressure in a range of 1–10² mTorr after the etchant gasses are injected into the chamber. The ICP source generates a high-density plasma due to inductive coupling between the ICP generator and the plasma. The ICP generator, located in the plasma generation region, creates an alternating RF magnetic field and induces an RF electric field that accelerates electrons participating in the ionization of gas molecules and atoms at low pressure. A separate CCP generator applies RF power to the electrode below the substrate, which helps to form a DC bias voltage. This negative potential attracts the ions out of the plasma discharge region and controls the ion energy. Consequently, the plasma density and the ion bombardment energy can be adjusted separately by tuning the ICP

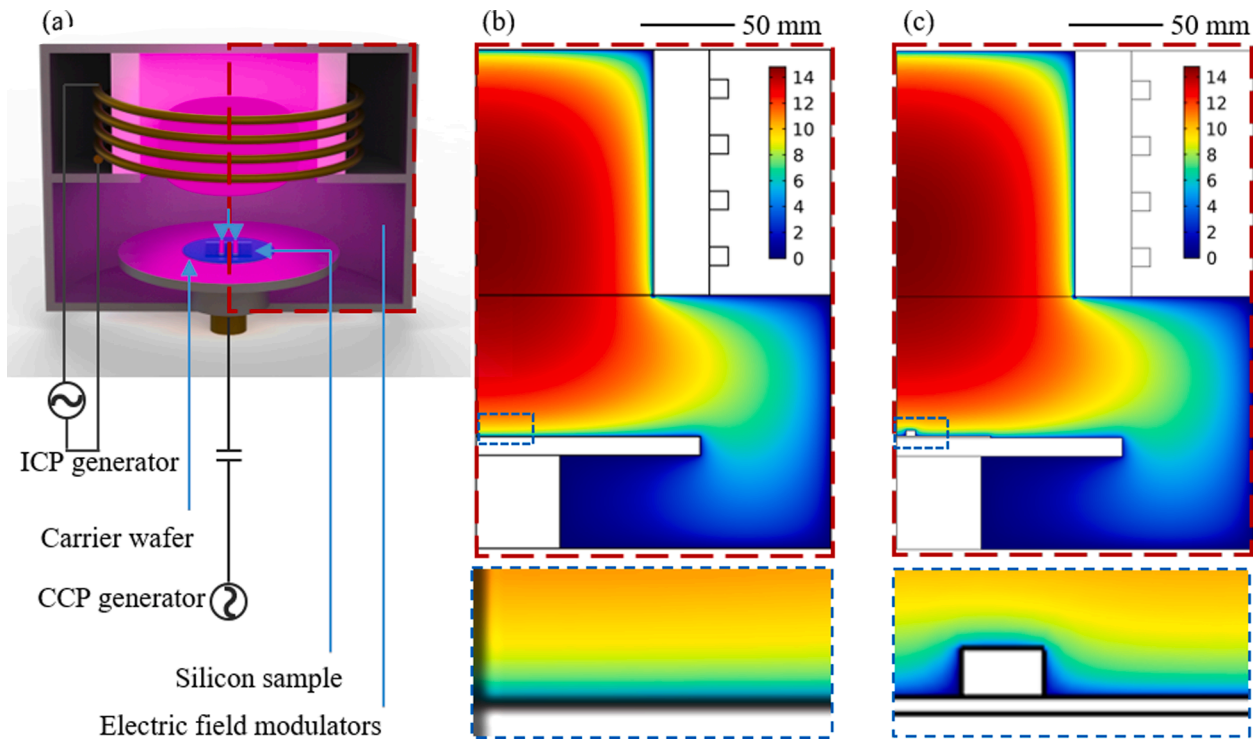


Fig. 2. (a) Schematic of an ICP etcher with both ICP & CCP generators. (b) Electric potential in the plasma chamber without a sample or electric field modulator. (c) Electric potential in the plasma chamber in presence of a silicon substrate and a set of electric field modulators.

and CCP power generators [32,33].

A typical plasma chamber with RF generators is represented in Fig. 2 (a). Fig. 2(b) shows the electric field inside the plasma chamber during an etching process without the sample or the electric field modulators, while Fig. 2(c) shows the electric field with presence of the sample and a set of electric field modulators. It is noticeable that the electric field is only distorted locally near the sample surface, and this is the key feature to achieve the tilted etching. Therefore, we focus on the study of the near sample surface region. Since the electrode is isolated from the ground, the electrons accumulate on the surface of the electrode and the sample, thus the electrode gains a negative potential. The plasma body is then no longer neutral due to the imbalance of ion and electron charging, and the potential is normally a few volts above zero. The electron-less space between the plasma body and the electrode surface is called sheath region [34]. The sheath is a thin layer that can be defined by its typical thickness and the voltage drop between its edge and wall [35,36]. Particle collisions rarely happen in the sheath region, and the plasma formation is inhibited in this space due to the lack of electrons, therefore it visually appears as a dark space [37,38]. The sheath thickness is usually in the range of few Debye lengths [35,36]. Due to the potential drop within the sheath region, the ions can be accelerated and gain kinetic energy. This ion momentum triggers the anisotropic etching, and the incident angle of the ions should dominate the actual etching direction. The sheath dynamics controls the energy and the angular distribution of ions bombarding the electrode, which in turn affects the surface reaction rate and the walls profile of microscopic features etched into a wafer resting on the electrode [38].

2.2. Pattern preparation

A series of sample chips are etched and measured to study how the electric field modulators affect the etching result, including cases of electric field modulation in 1-D for periodic linear patterns and 2-D for chessboard like patterns. 4-inch N-type <100> Si double side polished wafers were used for the preparation of sample chips, and the wafers are

250 μm thick. We normally use low resistivity wafers (0.001–0.01 $\Omega\text{ cm}$) for the convenience of following the trench filling process [9]. First, the wafer was coated with a 50 nm layer of Cr, which works as hard mask during the DRIE process. For the case of 1-D tilting test, a pattern of periodic lines was realized by photolithography. A layer of AZ BARLi-II anti-reflective layer was spin-coated on top of the Cr layer at a speed of 4000 rpm, and then soft baked with a hot plate at 180 $^{\circ}\text{C}$ for 60 s. SUMIRESIST PFI-88A7 was spin-coated at a speed of 4000 rpm and soft baked on hot plate at 90 $^{\circ}\text{C}$ for 60 s. The exposure was realized by displacement Talbot lithography method [39,40] with an Eulitha PhableR200 system, using a 377 nm wavelength polarized laser light source. A quartz photomask with a period of 4 μm generated a Talbot carpet with a period of 2 μm , and the Talbot distance of this Talbot carpet is calculated with Eq. (1),

$$Z_t = \frac{\lambda}{1 - \sqrt{1 - \frac{\lambda^2}{p_{\text{mask}}^2}}} \quad (1)$$

where Z_t is the Talbot distance, is the wavelength of the light source, and p_{mask} is the period of the linear pattern on the photomask. The scanning range of the exposure was 170 μm , corresponding to twice the Talbot distance, for the purpose of mitigating the ‘beating effect’ [39]. The exposure time was 200 s, in order to have a 0.5 duty cycle in the pattern. The wafer was post-exposure baked on a hot plate at 110 $^{\circ}\text{C}$ for 60 s and then developed with Megaposit MF-24A. The bottom anti-reflective layer was etched away in an Oxford RIE etcher with $\text{CHF}_3/\text{O}_2/\text{Ar}$ mixture as etchant gas. For the case of 2-D test, a chess-like pattern was realized with square side of 2 μm . A layer of MICROPOSIT S1805 photoresist was spin-coated on top of the Cr layer at a speed of 4000 rpm and exposed with a SUSS MA6 mask aligner in vacuum contact mode after the photoresist baking at 115 $^{\circ}\text{C}$ for 90 s. The development was performed in Megaposit MF-24A. For both 1-D and 2-D tests, the patterns were transferred into the Cr layer by plasma etching using Cl_2/O_2 mixture as etchant gas.

2.3. Experimental kit preparation

An experimental kit is composed of a carrier wafer, a patterned chip and an electric field modulator, whose assembly is schematically showed in Fig. 3. A $60 \times 60 \text{ mm}^2$ sized chip was precisely cleaved from the patterned 4-inch wafers. A 4-inch N-type (100) Si single side polished wafer with a thickness of $525 \mu\text{m}$ was used as carrier wafer for each experiment set. The carrier wafers were thermally oxidized in a diffusion oven. If the SiO_2 layer gets fully etched away, the Si substrate underneath will be exposed to the plasma consuming the etchant from and leading to an early stop of the trench etching. In this study, the thickness of the SiO_2 layer is $2 \mu\text{m}$, which is sufficient to endure the whole Bosch etching process for the targeted depth. First, the chip was

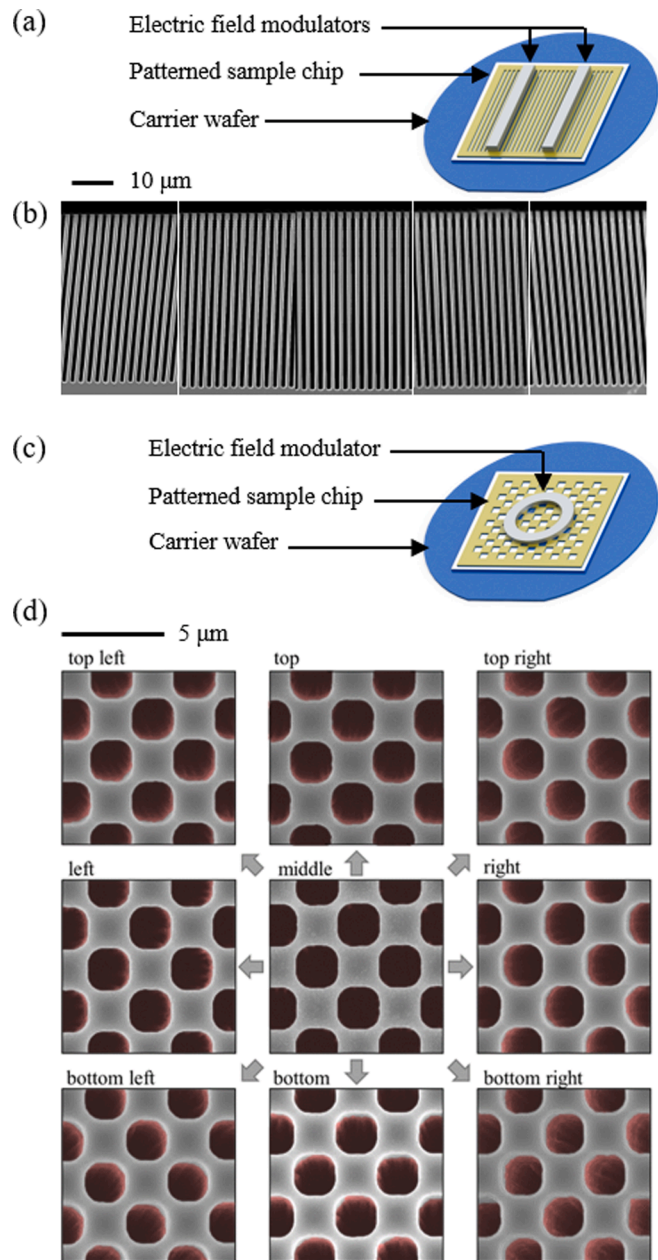


Fig. 3. (a) Schematic of the 1D-experimental kit: arrangement of carrier wafer, patterned sample and electric field modulators for the 1D-tilted etching. (b) SEM images in cross section of the 1D-tilted linear grating with pitch $2 \mu\text{m}$. (c) Schematic of 2D-experimental kit: arrangement of carrier wafer, patterned sample and electric field modulators for the 2D-tilted etching. (d) SEM images in top view of the 2D-tilted chess-like grating.

attached in the center of the carrier wafer with a layer of insulating bonding wax. Then, a set of electric field modulators were located on top of the sample chip and glued by the bonding wax. For the case of 1-D test, the electric field modulators were Al slabs. The Al slabs have a length (l) of 50 mm and a width of 5 mm and they are placed with the length parallel to the lines in the pattern. Four pairs of Al slabs were used in the experiment with slab thickness (h) of $3, 2, 1,$ and 0.5 mm . One sample chip was prepared with each pair of Al slabs, and the slabs were placed at a distance (d) of 10 mm in order to study the influence of the electric field modulator thickness. For the case of $h = 0.5 \text{ mm}$, three chips were prepared with d of $15, 20,$ and 25 mm , in order to study the influence of the distance between the two electric field modulators. The thickness and the distance are the major factors affecting the etching results. Fig. 3(a) schematically shows how the components of the 1-D experiment set were arranged. For the case of 2-D test, the electric field modulator is an Al ring. The Al ring has an inner diameter of 15 mm and an outer diameter of 35 mm . The thickness of the Al ring is 3 mm . Fig. 3(c) schematically shows how the components of the 2-D experiment set were arranged.

2.4. DRIE process

The prepared experimental sets are etched in an Oxford Plasma-LabSystem100 ICP etcher. The etching gas is SF_6 and the passivation layer forming gas is C_4F_8 . The Bosch process is a time-multiplex process with etching and deposition steps start alternately. In this study, the Bosch process always starts with a deposition step to form a protective layer, and ends with an etching step to avoid too much residual polymers in the etched trenches. For the one dimensional test, we choose an etching conditions with low chamber pressure and low RF power, since the convection inside the trenches is insufficient due the small trench width of 500 nm [10]. For the etching of one dimensional linear gratings, the chamber pressure was maintained at 15 mTorr , the etchant gas flows were SF_6 (90 sccm)/ C_4F_8 (5 sccm) and SF_6 (5 sccm)/ C_4F_8 (90 sccm) during the etch and deposition steps, and the RF powers were ICP (30 W)/RF (700 W). For the two dimensional case the square holes opening side is $2 \mu\text{m}$, i.e. four times larger than the trenches. Therefore, a more conservative recipe was used compared to the linear gratings with the same period. The chamber pressure was maintained at 20 mTorr ; the etchant gas flows were SF_6 (95 sccm)/ C_4F_8 (5 sccm) and SF_6 (10 sccm)/ C_4F_8 (90 sccm) during the etch and deposition steps; the RF powers were ICP (50 W)/RF (800 W). The DC bias voltage $V_{dc} = -160 \text{ V}$ is indicated during the etching steps. For both one dimensional and two dimensional cases, the trenches are etched into the Si substrate to depths in a range of $15\text{--}40 \mu\text{m}$.

2.5. SEM examination and tilted angle measurement

The etched chips are taken off from the carrier wafer for further examination. For one dimensional tests, the chips are cleaved along the direction perpendicular to the grating lines. Cross sectional scanning electron microscope (SEM) images are taken with a Zeiss Supra VP55 system at a magnification of 5 kX . Fig. 3(b) shows an example of a series of SEM images taken from a 1-D tilting etched sample at different positions x . The tilted angles of the trenches are measured from the SEM images with a measurement accuracy of $\pm 0.2^\circ$. The position x is measured in reference to the SEM stage position with a measurement accuracy of $\pm 0.2 \text{ mm}$.

For the 2-D test, the SEM images are realized in top view. Fig. 3(d) shows the top view SEM images taken from several different areas on the two dimensional fan-shaped etched sample, at a magnification of 10 kX . The etching direction in each imaging area can be recognized by observing the sidewall conditions (dyed with red color in Fig. 3(d)). For example, in the bottom right subplot of Fig. 3(d), only the top left parts of the hole sidewalls can be seen, indicating that the etching direction is towards the bottom right of the sample.

3. Simulation of ion trajectory

We used COMSOL software to simulate the chamber electric field during an etching process. We used the geometry of an Oxford PlasmaLabSystem100 etcher chamber for building the model. A schematic is showed in Fig. 2(a). The parameters of our Bosch process are the initial conditions for the time transient simulation. For simplicity, the chamber is treated as sealed without considering the gas convection.

The simulation of the local electric field near the sample surface is done with the PDE (partial differential equation) tool of Matlab© based on the real arrangement and geometry of the sample and the electric field modulators, using a triangular shaped mesh for the model. The width of the simulation zone is 50 mm, and the height of the simulation zone is the sheath thickness plus the modulator height. The etching process used this study has a relatively low chamber pressure of 15–20 mTorr, therefore we assume that the sheath thickness has a value of 3 mm [41]. A collisionless sheath is assumed following the Child–Langmuir law [42,43]. Collisionless path is realized in a low-pressure plasma regime, the mean free path under our experimental conditions has the same order of magnitude of the Debye sheath thickness. The mean free path l of pure SF₆ is calculated using with Eq. (2):

$$l = \frac{k_B T}{\sqrt{2\pi} d^2 p} \# \quad (2)$$

where k_B is the Boltzmann constant, T is the temperature of the gas, πd^2 is the effective cross-sectional area for spherical particles, and p is the pressure. The calculated value is $l = 1.4$ mm, assuming pure SF₆ gas at cold ion temperature of $T = 0^\circ\text{C}$ and a pressure of $p = 15$ mTorr, the calculated l is about half of the Debye sheath thickness (3 mm). However, this mean free path value is just an upper limit. Indeed, in the plasma bulk, once the SF₆ molecules are ionized into smaller ions, electrons, and radicals, the average kinetic diameter will decrease, leading to an increase of the mean free path l . Moreover, the kinetic energy of the ions escaping from the plasma bulk and entering in the sheath is $E_k = \frac{1}{2} M \times v_{\text{bohm}}^2$: significantly higher than the thermal energy of a gas. Furthermore, due to the loss of ions and electrons in the sheath region, there will be a pressure gradient existing at the sheath edge at dynamic equilibrium [44]. Since the chamber pressure is measured at the chamber walls, the actual pressure within the sheath region is lower than the measured pressure.

The upper boundary condition is set as ‘Dirichlet’ type [45], and the value equals to the plasma potential V_{pp} at the corresponding position. The plasma body is almost electrically neutral, so we set V_{pp} as zero. The lower boundary condition is also ‘Dirichlet’ type, and the value equals to the DC bias voltage V_{dc} . The two side boundary conditions are ‘Neumann’ type [45]. The maximum element size h_{max} is set as 0.01 mm to have a fine enough mesh with a relative affordable computing power. The PDEs are then solved at each node by Matlab. The calculated values on the nodes are used to track the moving trajectory and momentum of the ions. The tracking is done as follows: an ion travels randomly in the plasma body at a thermal velocity, the ion is attracted and accelerated under the influence of the electric field when it enters the sheath region, moving towards the electrode. The ion enters the simulation region from point $T(x_0, y_0)$ with an initial velocity v_{init} . Normally the ion temperature of glow discharge plasma is in the range of 300–1000 K [34]. Since the v_{init} module is already in the range of few ten thousand meters per second [46], which is much larger in comparison to the thermal velocity of the ions in the plasma body, the horizontal component of v_{init} is set at an mean value of 300 m/s and we can assume that the ion enters the simulation region with a moving direction perpendicular to the sample chip. The total sampling number of the ion positions in vertical direction is 20, so we follow Eq. (3) to calculate the Y position of the ion:

$$T_{y,n+1} = T_{y,n} + \Delta y \# \quad (3)$$

where $T_{y,n}$ is the n^{th} position of the ion on Y-axis, $T_{y,n+1}$ is the next

position of the ion on Y-axis, and Δy is the distance between two positions on Y-axis and is calculated as the reciprocal of the sample rate. In order to describe the ion moving trajectory under the influence of the local morphology near the sample surface, the instantaneous moving direction of the ion is forced by the potential gradient [47]. Since the potential inside the simulation region is calculated with finite element method, and the h_{max} is approximately ten times smaller than Δy , the potential $U(x', y')$ at the nearest node $T(x', y')$ in the mesh is used for the calculation of the instantaneous moving direction of the ion at position $T(x, y)$. The acceleration of the ions in X and Y directions are calculated with Eq. (4) and Eq. (5):

$$a_{y,n} = \frac{dU_n}{dy} \frac{Q}{M} \# \quad (4)$$

$$a_{x,n} = \frac{dU_n}{dx} \frac{Q}{M} \# \quad (5)$$

where $a_{x,n}$ and $a_{y,n}$ are the instantaneous acceleration of the ion at n^{th} position on the X-/Y-axis; dU_n/dx and dU_n/dy are the potential gradient in X and Y-axis, respectively, at the n^{th} position of the ion, which can be obtained by solving the partial differential equations in the model; Q/M is the charge mass ratio of the tracked ion. The travelling time $t_{n \rightarrow (n+1)}$ of the ion from the n^{th} position to the $(n+1)^{\text{th}}$ position is calculated with Eq. (6):

$$t_{n \rightarrow (n+1)} = \frac{\sqrt{2a_{y,n}\Delta y + v_{y,n}^2} - v_{y,n}}{a_{y,n}} \# \quad (6)$$

where $v_{y,n}$ is the y component of the instantaneous velocity of the ion at $(n+1)^{\text{th}}$ position in the Y-axis. The instantaneous velocities of the ion on X-/Y-axis at the next position are calculated with Eq. (7) and Eq. (8):

$$v_{y,n+1} = v_{y,n} + a_{y,n} \cdot t_{n \rightarrow (n+1)} \# \quad (7)$$

$$v_{x,n+1} = v_{x,n} + a_{x,n} \cdot t_{n \rightarrow (n+1)} \# \quad (8)$$

The next position of the ion in X-axis is calculated with Eq. (9):

$$T_{x,n+1} = T_{x,n} + v_{x,n} \cdot t_{n \rightarrow (n+1)} + \frac{1}{2} a_{x,n} \cdot t_{n \rightarrow (n+1)}^2 \# \quad (9)$$

where $T_{x,n+1}$ is the $(n+1)^{\text{th}}$ position of the ion in the X-axis, and $T_{x,n}$ is the n^{th} position of the ion on X-axis.

The instantaneous velocity and acceleration as function of position are reported Figure S1 of Supplementary material.

Finally, the incident angle θ_i of this ion at the surface of the sample chip is calculated with Eq. (10):

$$\theta_i = \arctan\left(\frac{|v_{x, \text{end}}|}{|v_{y, \text{end}}|}\right) \# \quad (10)$$

where $v_{x, \text{end}}$ ($v_{y, \text{end}}$) is the horizontal (vertical) component of the ion instantaneous velocity when it arrives at the surface of the sample chip. Fig. 4 reports an example of ion trajectory calculation. The ion follows a parabolic moving trajectory between T_n and T_{n+1} , and the accuracy of the simulation results is affected by the distance between the sampling points, therefore a higher sampling rate is preferred.

The moving trajectories and the velocities of 51 ions are tracked along the upper boundary, and only those ions that arrived at the surface of the sample chip are used for the final plot of the incident angle distribution.

4. Results and discussion

The modulator affects only locally the ion trajectories (see Fig. 2c, Fig. 4 and Fig.S1). The ion trajectory is deflected from the vertical direction as a function of the modulator geometry, the trajectories of the ions approaching the central position of the chip remain almost straight,

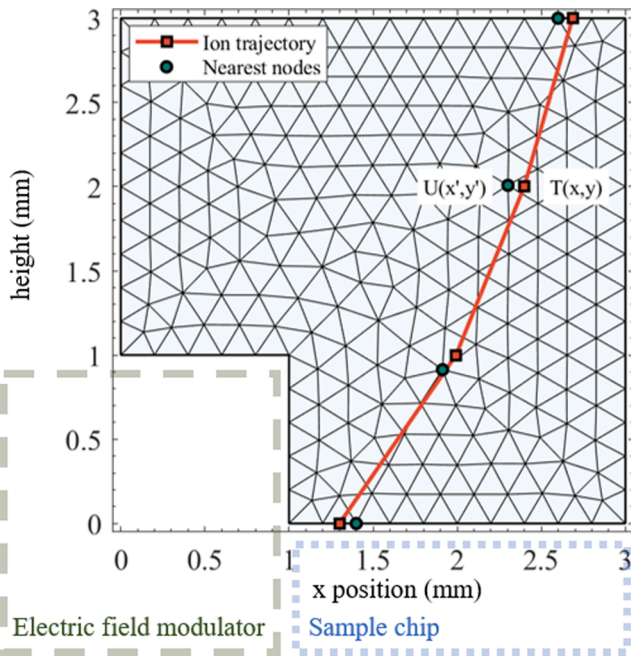


Fig. 4. Method for an ion trajectory tracking and incident angle calculation. Square symbols are sampling points. The potential gradient acquired from the nearest node of the mesh is used to calculate the ion direction before it reaches the next sampling point, and the accumulated kinetic energy and the acceleration direction according to Eqs. (3) and (4) in the text. The profiles of the electric field modulator and the sample chip are sketched.

gaining a very small lateral momentum. Ions that approach the sample surface region close to the electric field modulator are strongly deflected, and some even collide with the electric field modulator instead of arriving at the sample chip surface. In contrast to a single side modulation with dielectric material [48,49], the symmetric design with metal modulators does not have huge local charge variation on the electric field modulators, and any sudden change in charge density on the modulator surface can be self-compensated thanks to the high electron mobility in metal. This allows a gradual change in the incident angles along the lateral direction of the sample surface perpendicular to the pattern lines, which is ideal for gratings used in XGI systems, as sketched in Fig. 2(b).

Ideally, in a XGI system, the grating lines should have tilted angles along the direction perpendicular to the grating lines (X axis) according to Eq. (11):

$$\theta_x = \arctan\left(\frac{x}{w}\right) \# \quad (11)$$

where θ_x is the tilt of the grating line at position x , with the X-axis in the plane of the silicon substrate and perpendicular to the grating lines (see Fig. 1d), and w is the distance between the focus point of the X-ray tube and the grating, w is usually in the order of few centimeters [12]. This tilt gradient produces a grating with a fan-shaped structure (Fig. 3b). Since the tilt is created during the etching, θ_x is evaluated as the ion incident angle at the ion arrival position x along the X-axis. Since the ions are accelerated before impinging on the grating pattern, the etching depth along each θ_x depends only on the etching time and all the grating lines (silicon lamellas) have the same height. This has been verified within the limitations of the SEM cross sections (Fig. 3b) and for the etching depth of maximum 40 μm and pitch size of 2 μm . Therefore, this kind of gratings are suitable for transmitting X-ray equal in all radial directions. The remaining thickness of the substrate varies with the distance to the central axis, but the attenuation of the transmitted X-ray is negligible, details are discussed in Supplementary material.

Fig. 5 reports the profile of equipotential lines and the ion

trajectories in a plane perpendicular to the substrate as a function of the distance x from the center of the pattern and for several modulators heights (h) and distances (d).

Fig. 6(a) shows the simulated and measured incident angle as a function of the position x on the etched sample in a plane perpendicular to the substrate. Cross sectional SEM images of the samples are available in Supplementary material. As a general trend: the thicker and the closer the electric field modulators, the larger the tilt gradient and the higher the maximum angle. When the modulators are far away from each other or thin enough, there is a weakly influenced area in the middle of the modulators, and the tilted angle varies as a bowl as a function of x . When the modulators are close or thick enough, the strong influence areas of the modulators overlap, leading to a linear tilted angle distribution.

We assumed a uniform potential, while a local potential can rise up during the etching due to the trench formation or the silicon substrate can produce a screening effect so introducing a local electric field. The potential distribution can also depend on the chamber geometry and can vary from etcher to etcher. The determination of the potential distribution at the Si sample surface is a general problem in DRIE machine design due to the lack of an efficient way of probing real potential conditions inside of the etcher chamber at micrometer scale during a plasma etching process. For example, the model should follow the Gauss's Law, therefore a simple parabolic potential distribution can be applied to the sample surface [50]. We used a potential distribution according to Eq. (12):

$$V_x = \frac{4kV_{dc}}{d^2}x^2 + (1-k) \times V_{dc} \# \quad (12)$$

where V_x is the potential at position x , k is a fitting parameter, d is the inter-modulators distance, V_{dc} is the bias potential during the etching. Eq. (12) describes a parabolic potential with a minimum number of parameters and assuming the boundary condition of V_{dc} at the modulator' edge.

Fig. 7(a) shows the comparison between a constant potential (left part of Fig. 7(a)) at the substrate and the local parabolic potential of Eq. (12) (right part of Fig. 7(a)) for a case of modulators with $h = 0.5$ mm and $d = 25$ mm. The fitting parameter k ($k = 0.25$) has been retrieved by the measured tilt distribution showed in Fig. 7(b).

The simulated tilted angles (Fig. 7b) approximate the measured values with a smaller deviation with respect to a constant potential case (Fig. 7a), especially for the larger inter-modulators distance. The parabolic potential distribution is still an idealized case. Without considering the electron exchange at the interface between the silicon substrate and the plasma, and the local defects in the silicon body, it is very hard to predict the real potential distribution. However, introducing an artificial parabolic potential demonstrates that the simulation can be enough accurate to reproduce the most relevant experimental features of strong tilt for all the conditions of modulator thickness (0.5–3 mm) and inter-modulators distance (10–25 mm). Therefore, the parabolic potential can be used as fitting parameter.

All in all, the model predicts the trend of the etching results, and can be used as a guideline for the processing design. A better approximation would require to simulate the screening effect of the silicon substrate by describing the potential distribution at the silicon surface with a stationary Poisson-Boltzmann equation where the charges' distribution in the semiconductor region is self-consistently related to the potential distribution of the composite system. However, as discussed, several still unknown parameters are necessary for the correct setting of the Poisson-Boltzmann equation in the semiconductor material. Several other secondary factors might also help to improve the simulation quality. The angle inaccuracy can be originated by several factors. Simulation inaccuracy can derive from an oversimplified model. The plasma etching process is an extremely complex process, hence the model has been simplified by introducing some assumptions (e.g. the potential at the sample surface follows a perfect parabolic distribution; the plasma conditions saturate instantly and keep stable during the whole process;

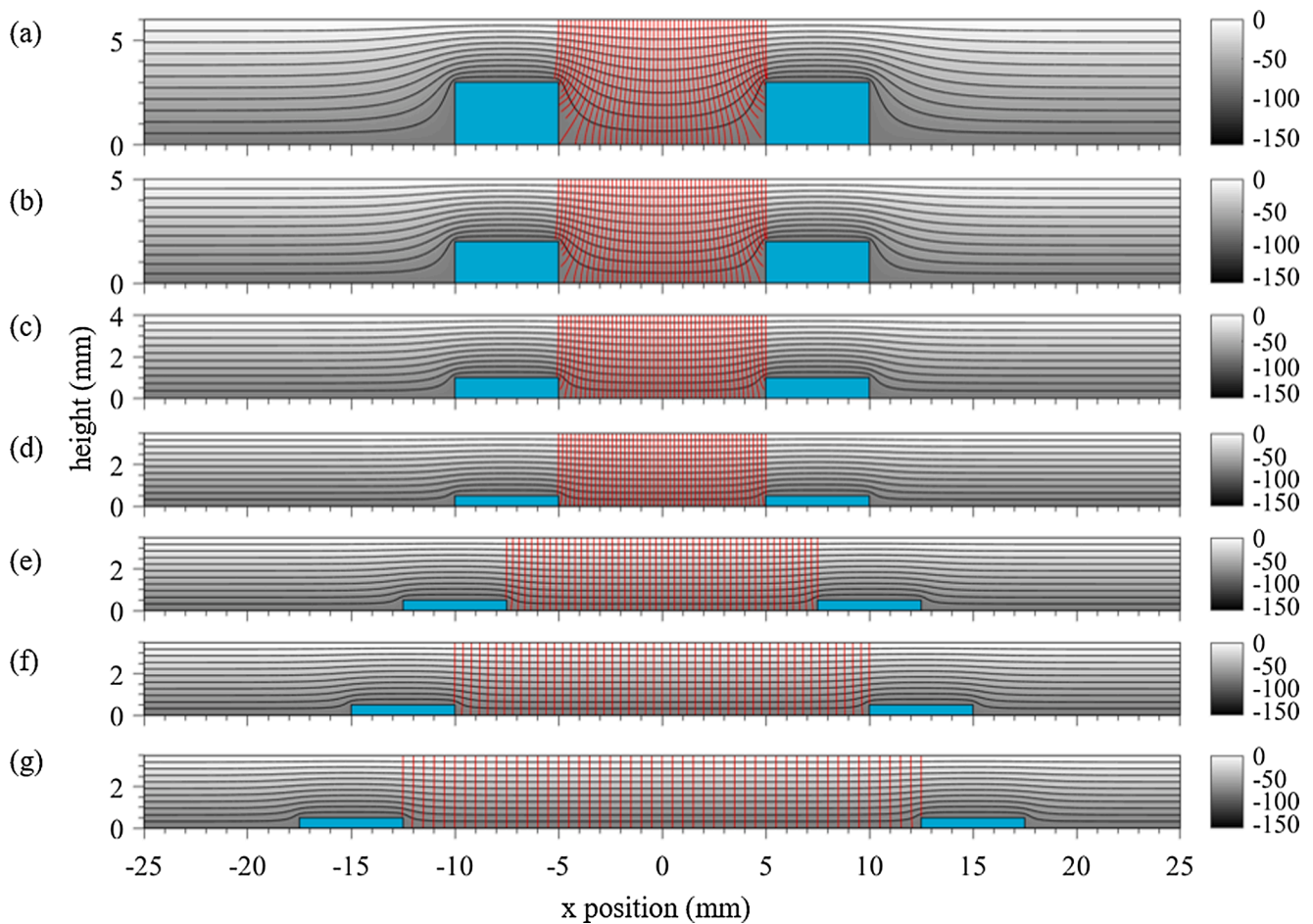


Fig. 5. Simulated equipotential lines of the electric field (black lines) and ion moving trajectory (red lines) of modulators with: (a) $h = 3$ mm, $d = 10$ mm; (b) $h = 2$ mm, $d = 10$ mm; (c) $h = 1$ mm, $d = 10$ mm; (d) $h = 0.5$ mm, $d = 10$ mm; (e) $h = 0.5$ mm, $d = 15$ mm; (f) $h = 0.5$ mm, $d = 20$ mm; (g) $h = 0.5$ mm, $d = 25$ mm. (For interpretation of the references to colour in this figure legend, the reader is referred to the web version of this article.)

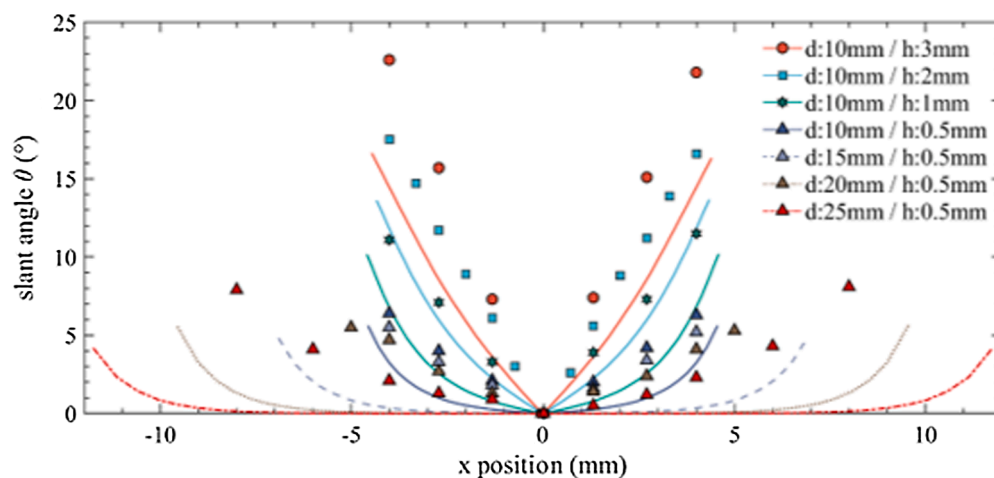


Fig. 6. Simulated (lines) and measured (symbols) ion incident angle (slant angle) θ vs position x . The simulations are plotted as lines, and the measurements are plotted as symbols. The difference in electric field modulator thickness (h) is distinguished with different line styles, and the difference in the distance (d) between the two electric field modulators is distinguished with different symbols.

the plasma body has a sharp and flat edge, and etc.), and some secondary factors have been ignored (e.g. higher order ionization of the etchants, gas convection, the change in local electric field in the etched trenches, and etc.). Some systematic errors might have been introduced during the fabrication process and the measurement of the angles (e.g. the

misalignment of the experimental setup, the change of etcher conditions, the limited accuracy of the measurement instruments, and etc.). However, the symmetry of the measured angles with respect to the $x = 0$ axis seems to indicate that the systematic error should have had a minor impact. Future work will be dedicated to address this model

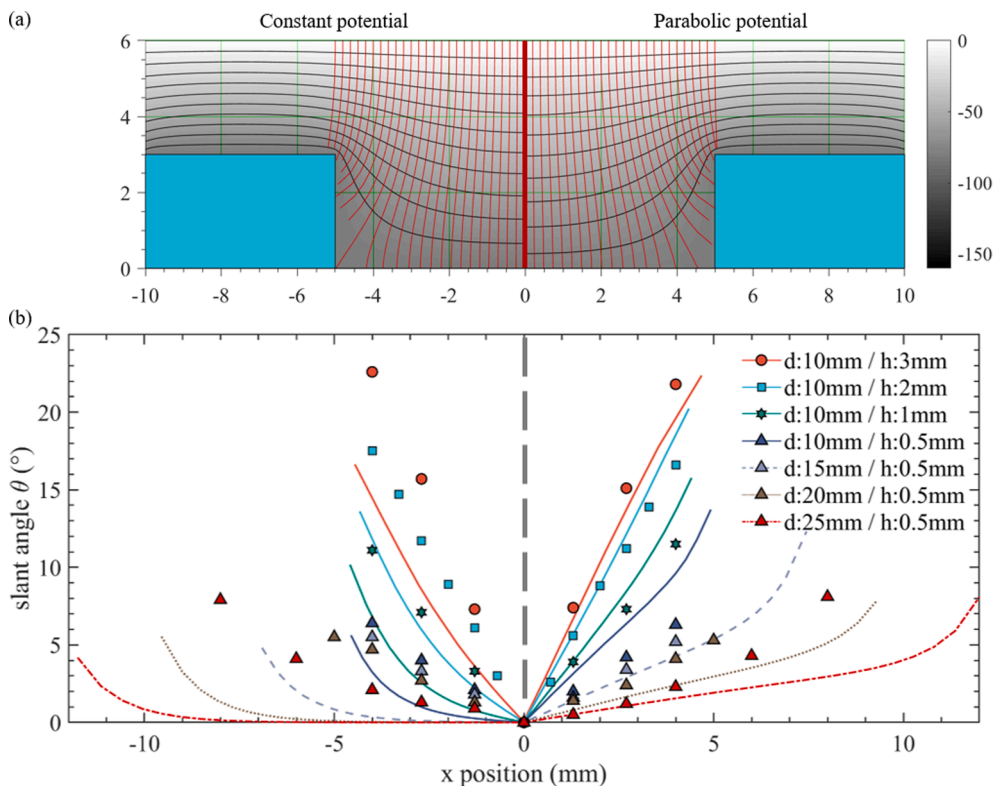


Fig. 7. (a) Simulated equipotential lines of the electric field (black lines) and ion moving trajectory (red lines) of modulators with $h = 0.5$ mm and $d = 25$ mm, under condition of a constant potential (left) or a parabolic potential distribution (right) at the surface of the sample. (b) Simulated (lines) and measured (symbols) ion incident angle (slant angle) θ vs position x , under condition of a constant potential (left, negative x) or a parabolic potential distribution (right, positive x) at the surface of the sample. Same plotting style of Fig. 6.

upgrade.

For imaging applications with XGI systems, the tilted angle gradient in the grating follows Eq. (10) and is almost linear since the system usually requires a maximum tilted angle of few degrees. Only when the thickness and the distance of the modulators are carefully balanced, the actual tilted angle follows a linear variation, symmetric over the center axis. However, not every application requires linear variation of the tilt, therefore the ‘bowl shaped’ tilted angle functions might be also interesting for other applications. Moreover, the tilt variation can be produced also with non-symmetric modulators. The design can also be meta symmetric or even one-side modulated for some other unique structures. Fig. 8 shows some examples of different modulator shapes and asymmetric modulators. We see that with symmetric design, the minimum tilting angle position always stays at the center of the system, while the maximum tilting angle value and the linearity of the angle distribution might change. With asymmetric design, not only the angle value and distribution, but also the minimum tilting angle position changes.

This study addressed the requirements of XGI systems [4,12], but the developed technology allows to bypass the limitations of planar micro-fabrication technology and can be extended to other complex X-ray optics, such as Laue lens [51], wavefront sensors [52], three-dimensional shaped tilted zone-plates [53].

5. Conclusions

Tilted etching with symmetric metal electric field modulator(s) was developed for the purpose of fabricating periodical nano-/micro-structure arrays in Si substrates. The role of the electric field modulator thickness and inter-modulators distance on the tilt gradient has been studied with a finite element method. The thicker the electric field modulators and the shorter the inter distance are, the larger is the tilt gradient and the higher the maximum angle. The etching behavior expected from the model has been experimentally verified by fabricating a series of samples with different modulator’s parameters. The influence of some critical factors such as the distribution of the bias potential at

the substrate has been indicated. This can be implemented in future works and potentially enable new ways to control the tilted etching. The model can be used to guide the design of the experimental setup with fan-shaped microstructures in 1D and 2D. We simulated the electrical field of few symmetric and asymmetric modulator’s slabs with different shapes, such as rectangular, triangular and round cross sections. The advantages of this technology include: (1) tilted structures with high aspect ratios can be fabricated during the plasma etching; (2) the tilted angles of the structures change gradually, so that certain functionalities can be achieved; (3) the tilted angles can be adjusted by using different sets of electric field modulators to meet different requirements.

We envisage implementing the proposed model to quantitatively predict the modulators design for a desired angle modulation. The etching results might vary a lot with using different etching tools because of the different chamber conditions, component arrangement, and the way of measuring the bias voltage (directly measured with a cylindrical Langmuir probe or calculated from the forwarded source/platen RF power). Therefore, a unified algorithm will require a parametrization of the specific etching tool.

We demonstrated a robust fabrication feasibility of slanted gratings with different experimental conditions, modulators size and shape by etching a series of 1D fan-shaped gratings with pitch size of $2\ \mu\text{m}$ and 2D tilted chess-board gratings with pitch size of $2\ \mu\text{m}$ and trench depths in a range of $15\text{--}40\ \mu\text{m}$. The proposed method can be used to design and micro-fabricate high aspect ratio slanted diffractive optics with a continuous angle gradient for several applications, such as X-ray imaging, augmented and virtual reality with visible light. Moreover, the method can be generalized to any etching plasma and substrates other than silicon.

CRedit authorship contribution statement

Zhitian Shi: Investigation, Conceptualization, Methodology, Validation, Visualization, Writing – original draft. **Konstantins Jefimovs:** Conceptualization, Methodology, Validation, Writing – review &

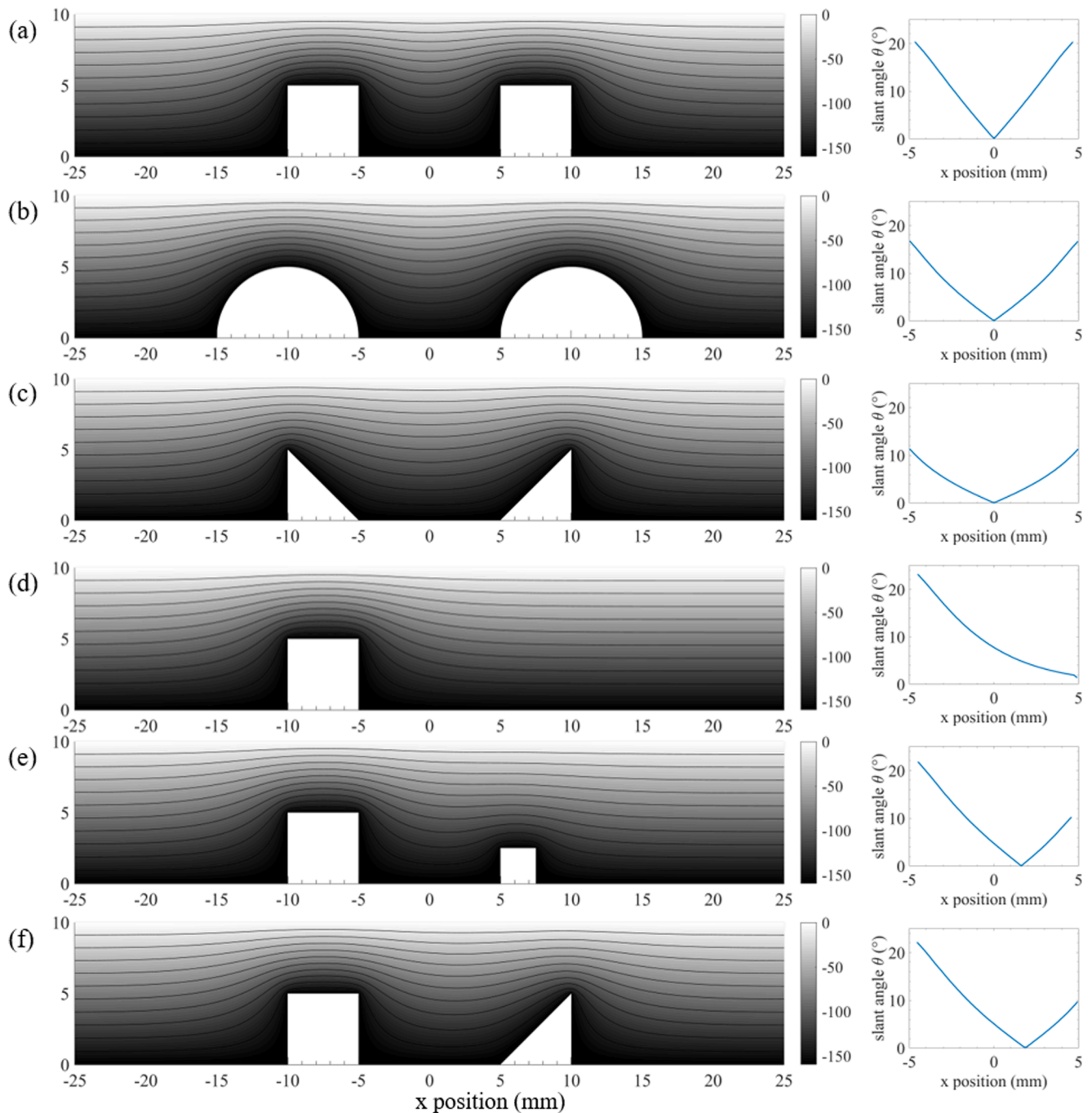


Fig. 8. Equipotential lines generated by different types of electric field modulators (left side), and corresponding slant angles along x axis (right side): (a–c) modulators with different shapes, (d) single-sided electric field modulation, (e) modulators with different sizes, and (f) modulators with different shapes. The modulators are showed in cross section, and horizontal axis indicates the distance in arbitrary units. The equipotential lines are showed in grey scale according to the potential gradient (gradient bar).

editing. **Antonino La Magna:** Validation, Writing – review & editing. **Marco Stampanoni:** Conceptualization, Validation, Writing – review & editing, Supervision. **Lucia Romano:** Conceptualization, Methodology, Validation, Writing – review & editing.

Declaration of Competing Interest

The authors declare that they have no known competing financial interests or personal relationships that could have appeared to influence the work reported in this paper.

Acknowledgments

This work has been partially funded by the ERC-2012-StG 310005 (PhaseX) grant, SNF_R'Equip grants 206021_189662 (SiDRY) and 206021_177036, the SNF-Sinergia Grants Nr. CRSII2_154472 and CRSII5_183568, the SNF Grant 159263, PHRT-grant CLARINET, the Fondazione Gelu and the SwissLOS Fond of the Kanton Aargau.

The authors would like to thank the LMN-PSI for providing the facilities and professional support.

Appendix A. Supplementary material

We report the details about: the instantaneous acceleration and velocity of ions within the simulation zone; the influence of tilt etching on X-ray transmission; a collection of cross section SEM images used to extract the measured data of Fig.6. Supplementary data to this article can be found online at <https://doi.org/10.1016/j.apsusc.2022.152938>.

References

- [1] J. Xiong, E.-L. Hsiang, Z. He, T. Zhan, S.-T. Wu, Augmented reality and virtual reality displays: emerging technologies and future perspectives, *Light Sci. Appl.* 10 (2021) 216.
- [2] T. Levola, P. Laakkonen, Replicated slanted gratings with a high refractive index material for in and outcoupling of light, *Opt. Express* 15 (2007) 2067–2074.
- [3] T. Levola, Diffractive optics for virtual reality displays, *J. Soc. Inform. Display* 14 (2006) 467–475.
- [4] T. Weitkamp, A. Diaz, C. David, F. Pfeiffer, M. Stampanoni, P. Cloetens, E. Ziegler, X-ray phase imaging with a grating interferometer, *Opt. Express* 13 (2005) 6296–6304.
- [5] V. De Andrade, V. Nikitin, M. Wojcik, A. Deriy, S. Bean, D. Shu, T. Mooney, K. Peterson, P. Kc, K. Li, S. Ali, K. Fezzaa, D. Gürsoy, C. Arico, S. Ouendi, D. Troadec, P. Simon, F. De Carlo, C. Lethien, Fast X-ray Nanotomography with Sub-10 nm Resolution as a Powerful Imaging Tool for Nanotechnology and Energy Storage Applications, *Adv. Mater.* 33 (2021), 2008653.
- [6] C. Arboleda, Z. Wang, K. Jefimovs, T. Koehler, U. Van Stevendaal, N. Kuhn, B. David, S. Prevrhal, K. Lång, S. Forte, R.A. Kubik-Huch, C. Leo, G. Singer, M. Marcon, A. Boss, E. Roessl, M. Stampanoni, Towards clinical grating-interferometry mammography, *Eur. Radiol.* 30 (2020) 1419–1425.
- [7] J. Vila-Comamala, L. Romano, K. Jefimovs, H. Dejea, A. Bonnini, A.C. Cook, I. Planinc, M. Cikes, Z. Wang, M. Stampanoni, High sensitivity X-ray phase contrast imaging by laboratory grating-based interferometry at high Talbot order geometry, *Opt. Express* 29 (2021) 2049–2064.
- [8] D. Josell, Z. Shi, K. Jefimovs, L. Romano, J. Vila-Comamala, T.P. Moffat, Pushing the limits of bottom-up gold filling for X-ray grating interferometry, *J. Electrochem. Soc.* 167 (2020), 132504.
- [9] K. Jefimovs, J. Vila-Comamala, C. Arboleda, Z. Wang, L. Romano, Z. Shi, M. Kagias, M. Stampanoni, Fabrication of X-ray Gratings for Interferometric Imaging by Conformal Seedless Gold Electroplating, *Micromachines* 12 (2021) 517.
- [10] Z. Shi, K. Jefimovs, L. Romano, M. Stampanoni, Towards the fabrication of high-aspect-ratio silicon gratings by deep reactive ion etching, *Micromachines* 11 (2020).
- [11] A.P. Sauter, J. Andrejewski, F. De Marco, K. Willer, L.B. Gromann, W. Noichl, F. Kriner, F. Fischer, C. Braun, T. Koehler, F. Meurer, A.A. Fingerle, D. Pfeiffer, E. Rummeny, J. Herzen, F. Pfeiffer, Optimization of tube voltage in X-ray dark-field chest radiography, *Sci. Rep.* 9 (2019) 8699.
- [12] Z. Shi, K. Jefimovs, L. Romano, J. Vila-Comamala, M. Stampanoni, Laboratory X-ray interferometry imaging with a fan-shaped source grating, *Opt. Lett.* 46 (2021) 3693–3696.
- [13] T. Thuring, P. Modregger, T. Grund, J. Kennntner, C. David, M. Stampanoni, High resolution, large field of view x-ray differential phase contrast imaging on a compact setup, *Appl. Phys. Lett.* 99 (2011), 041111.
- [14] T. Thuring, S. Hämmerle, S. Weiss, J. Nüesch, J. Meiser, J. Mohr, C. David, M. Stampanoni, Compact hard X-ray grating interferometry for table top phase contrast micro CT, *Proc.SPIE* (2013).
- [15] J.-K. Lee, S.-H. Lee, J.-H. Min, I.-Y. Jang, C.-K. Kim, S.H. Moon, Oblique-directional plasma etching of Si using a faraday cage, *J. Electrochem. Soc.* 156 (2009) D222.
- [16] K. Sugiura, S. Takahashi, M. Amano, T. Kajiyama, M. Iwayama, Y. Asao, N. Shimomura, T. Kishi, S. Ikegawa, H. Yoda, Ion beam etching technology for high-density spin transfer torque magnetic random access memory, *J. J. Appl. Phys.* 48 (2009) 08HD02.
- [17] H. Kitani, N. Toyoda, J. Matsuo, I. Yamada, Incident angle dependence of the sputtering effect of Ar-cluster-ion bombardment, *Nucl. Instrum. Methods Phys. Res., Sect. B* 121 (1997) 489–492.
- [18] C. David, J. Bruder, T. Rohbeck, C. Grünzweig, C. Kottler, A. Diaz, O. Bunk, F. Pfeiffer, Fabrication of diffraction gratings for hard X-ray phase contrast imaging, *Microelectron. Eng.* 84 (2007) 1172–1177.
- [19] L. Romano, M. Stampanoni, Microfabrication of X-ray optics by metal assisted chemical etching: a review, *Micromachines* 11 (2020) 589.
- [20] R. Barnett, D. Thomas, Y. Song, D. Tossell, T. Barrass, O. Ansell, A new plasma source for next generation MEMS deep Si etching: Minimal tilt, improved profile uniformity and higher etch rates, in: 2010 Proceedings 60th Electronic Components and Technology Conference (ECTC), 2010, pp. 1056–1059.
- [21] J.P. Gambino, S.A. Adderly, J.U. Knickerbocker, An overview of through-silicon-via technology and manufacturing challenges, *Microelectron. Eng.* 135 (2015) 73–106.
- [22] Y. Luo, J. Shao, S. Chen, X. Chen, H. Tian, X. Li, L. Wang, D. Wang, B. Lu, Flexible capacitive pressure sensor enhanced by tilted micropillar arrays, *ACS Appl. Mater. Interfaces* 11 (2019) 17796–17803.
- [23] W. Zhou, S. Liu, W. Liu, C. Zhang, Y. Li, W. Xu, K.S. Hui, Novel dry metal electrode with tilted microstructure fabricated with laser micromilling process, *Sens. Actuata. A* 264 (2017) 76–83.
- [24] R. Wang, F. Wu, F. Yu, J. Zhu, X. Gao, L. Jiang, Anti-vapor-penetration and condensate microdrop self-transport of superhydrophobic oblique nanowire surface under high subcooling, *Nano Res.* 14 (2021) 1429–1434.
- [25] B. Wu, A. Kumar, S. Pamarthy, High aspect ratio silicon etch: A review, *J. Appl. Phys.* 108 (2010), 051101.
- [26] S. Tachi, K. Tsujimoto, S. Okudaira, Low-temperature reactive ion etching and microwave plasma etching of silicon, *Appl. Phys. Lett.* 52 (1988) 616–618.
- [27] F. Laermer, A. Schilp, Method of anisotropically etching silicon, in: Robert Bosch GmbH, 1996.
- [28] X. Wang, W. Zeng, G. Lu, O.L. Russo, E. Eisenbraun, High aspect ratio Bosch etching of sub-0.25µm trenches for hyperintegration applications, *J. Vac. Sci. Technol. B Microelectron Nanometer Struct. Process Meas. Phenom.* 25 (2007) 1376–1381.
- [29] F. Laerme, A. Schilp, K. Funk, M. Offenberg, Bosch deep silicon etching: improving uniformity and etch rate for advanced MEMS applications, in: Technical Digest. IEEE International MEMS 99 Conference. Twelfth IEEE International Conference on Micro Electro Mechanical Systems (Cat. No.99CH36291), 1999, pp. 211–216.
- [30] F. Laermer, A. Urban, Challenges, developments and applications of silicon deep reactive ion etching, *Microelectron. Eng.* 67–68 (2003) 349–355.
- [31] R.A. Stewart, P. Vitello, D.B. Graves, E.F. Jaeger, L.A. Berry, Plasma uniformity in high-density inductively coupled plasma tools, *Plasma Sources Sci. Technol.* 4 (1995) 36–46.
- [32] V.A. Godyak, Electrical and plasma parameters of ICP with high coupling efficiency, *Plasma Sources Sci. Technol.* 20 (2011), 025004.
- [33] M.D. Henry, ICP etching of silicon for micro and nanoscale devices, in: California Institute of Technology, 2010.
- [34] K. Nojiri, Mechanism of Dry Etching, in: K. Nojiri (Ed.), *Dry Etching Technology for Semiconductors*, Springer International Publishing, Cham, 2015, pp. 11–30.
- [35] R.N. Franklin, Whereisthe sheath edge ? *J. Phys. D: Appl. Phys.* 37 (2004) 1342–1345.
- [36] E. Faudot, J. Ledig, J. Moritz, S. Heurax, N. Lemoine, S. Devaux, Experimental measurements of the RF sheath thickness with a cylindrical Langmuir probe, *Phys. Plasmas* 26 (2019), 083503.
- [37] H.S. Butler, G.S. Kino, Plasma sheath formation by radio-frequency fields, *Phys. Fluids* 6 (1963) 1346–1355.
- [38] T. Panagopoulos, D.J. Economou, Plasma sheath model and ion energy distribution for all radio frequencies, *J. Appl. Phys.* 85 (1999) 3435–3443.
- [39] Z. Shi, K. Jefimovs, L. Romano, M. Stampanoni, Optimization of displacement Talbot lithography for fabrication of uniform high aspect ratio gratings, *Jpn. J. Appl. Phys.* 60 (2021) SCCA01.
- [40] J. Konstantins, R. Lucia, V.-C. Joan, K. Matias, W. Zhentian, W. Li, D. Christian, S. Harun, S. Marco, High-aspect ratio silicon structures by displacement Talbot lithography and Bosch etching, *Proc. SPIE* (2017).
- [41] R.J.M.M. Snijkers, The Sheath of an RF Plasma : Measurements and Simulations of the Ion Energy Distribution, Technische Universiteit Eindhoven, Eindhoven, 1993.
- [42] R.T. Farouki, M. Dalvie, L.F. Pavarino, Boundary-condition refinement of the Child-Langmuir law for collisionless dc plasma sheaths, *J. Appl. Phys.* 68 (1990) 6106–6116.
- [43] S.B. Wang, A.E. Wendt, Sheath thickness evaluation for collisionless or weakly collisional bounded plasmas, *IEEE Trans. Plasma Sci.* 27 (1999) 1358–1365.
- [44] B. Scheiner, S.D. Baalrud, B.T. Yee, M.M. Hopkins, E.V. Barnat, Theory of the electron sheath and presheath, *Phys. Plasmas* 22 (2015), 123520.
- [45] S. Mazumder, Chapter 2 - The Finite Difference Method, in: S. Mazumder (Ed.), *Numerical Methods for Partial Differential Equations*, Academic Press, 2016, pp. 51–101.
- [46] M.J. Goeckner, J. Goree, T.E. Sheridan, Measurements of ion velocity and density in the plasma sheath, *Phys. Fluids B: Plasma Phys.* 4 (1992) 1663–1670.
- [47] S.G. Ingram, The influence of substrate topography on ion bombardment in plasma etching, *J. Appl. Phys.* 68 (1990) 500–504.
- [48] S. Murakawa, S. Fang, J.P. McVittie, Ion trajectory distortion and profile tilt by surface charging in plasma etching, *Appl. Phys. Lett.* 64 (1994) 1558–1560.
- [49] B. Chang, Oblique angled plasma etching for 3D silicon structures with wiggling geometries, *Nanotechnology* 31 (2019), 085301.
- [50] L.K. Kenneth, *Electrostatic Discharge*, first ed., CRC Press, 2005.
- [51] M. Joerg, B.S. Gregory, V. Stefan, Y. Wenbing, M. Albert, K. Hyon Chol, L. Chian, C. Ray, Multilayer Laue lenses as high-resolution x-ray optics, *Proc. SPIE* (2004).
- [52] Y. Liu, M. Seaberg, D. Zhu, J. Krzywinski, F. Seiboth, C. Hardin, D. Cocco, A. Aquila, B. Nagler, H.J. Lee, S. Boutet, Y. Feng, Y. Ding, G. Marcus, A. Sakdinawat, High-accuracy wavefront sensing for x-ray free electron lasers, *Optica* 5 (2018) 967–975.
- [53] S. Werner, S. Rehbein, P. Guttman, G. Schneider, Three-dimensional structured on-chip stacked zone plates for nanoscale X-ray imaging with high efficiency, *Nano Res.* 7 (2014) 528–535.